Published in partnership with Nanjing Tech University



https://doi.org/10.1038/s41528-024-00362-8

# Combustion-assisted low-temperature ZrO<sub>2</sub>/SnO<sub>2</sub> films for high-performance flexible thin film transistors

Check for updates

Bongho Jang <sup>1</sup>, Junil Kim<sup>1</sup>, Jieun Lee<sup>1</sup>, Geuntae Park<sup>1</sup>, Gyuwon Yang<sup>1</sup>, Jaewon Jang<sup>2,3</sup> & Hyuk-Jun Kwon <sup>1,4</sup>⊠

We developed high-performance flexible oxide thin-film transistors (TFTs) using  $SnO_2$  semiconductor and high-k  $ZrO_2$  dielectric, both formed through combustion-assisted sol-gel processes. This method involves the exothermic reaction of fuels and oxidizers to produce high-quality oxide films without extensive external heating. The combustion  $ZrO_2$  films were revealed to have an amorphous structure with a higher proportion of oxygen corresponding to the oxide network, which contributes to the low leakage current and frequency-independent dielectric properties. The  $ZrO_2/SnO_2$  TFTs fabricated on flexible substrates using combustion synthesis exhibited excellent electrical characteristics, including a field-effect mobility of 26.16 cm²/Vs, a subthreshold swing of 0.125 V/dec, and an on/off current ratio of 1.13  $\times$  106 at a low operating voltage of 3 V. Furthermore, we demonstrated flexible  $ZrO_2/SnO_2$  TFTs with robust mechanical stability, capable of withstanding 5000 cycles of bending tests at a bending radius of 2.5 mm, achieved by scaling down the device dimensions.

Flexible electronics have been applied to various fields, such as panel displays, sensors, and memory, leading to significant interest in new processing technologies and materials<sup>1,2</sup>. In particular, thin-film transistors (TFTs) are crucial components that enable the construction of electronic circuits on flexible substrates, and the development of TFTs with both highperformance and mechanical flexibility for flexible devices has been the subject of ongoing research in major areas<sup>3,4</sup>. Among several semiconductor candidates for flexible TFTs, polymers are known to have limitations due to their low mobility and poor environmental stability caused by H<sub>2</sub>O and O<sub>2</sub>, despite their low processing temperature and stable mechanical flexibility. In contrast, metal oxides have been considered prominent materials for TFT channels due to their high carrier mobility (even in the amorphous phase) and excellent optical transparency, attributed to their unique orbital structure and wide band gaps<sup>5</sup>. As a result, they have been recognized as attractive materials for the development of next-generation applications, such as high-resolution and high-frame-rate displays, as well as highperformance transparent and flexible electronics. In particular, interest in flexible oxide TFTs has notably increased with the development of flexible TFTs using a-IGZO, which has made significant advances in the active matrix display industry<sup>6</sup>. In the past few years, research on new metal oxides that do not include rare elements, such as In and Ga in a-IGZO, while achieving higher TFT mobility, has been gaining attention. Among various oxides, Sn-based oxides such as ITZO, IGTO, ZATO, and SnO<sub>2</sub> have demonstrated good electrical performance with high mobility and potential as alternative materials for oxide TFTs<sup>7-10</sup>. Sn<sup>4+</sup> has a similar electronic structure to In<sup>3+</sup>, is abundant and more cost-effective, so it can partially or completely replace In. Moreover, unlike Zn<sup>2+</sup> (284.1 kJ/mol), which is speculated to cause instability in TFTs due to weak bonding with oxygen, Sn<sup>4+</sup> (531.8 kJ/mol) demonstrates high bonding energy with oxygen<sup>11</sup>. SnO<sub>2</sub> can be a promising candidate due to its higher intrinsic mobility (250 cm²/Vs at 300 K) and wider bandgap (3.6 eV) compared to representative binary oxides such as In<sub>2</sub>O<sub>3</sub> and ZnO, and it has the lowest melting point related to process temperature among these materials<sup>12</sup>. Furthermore, to clearly elucidate the enhanced performance of Sn-based oxide TFTs, it is necessary to research SnO<sub>2</sub> as the starting material for these oxides.

From a processing perspective, oxide TFTs are compatible with various fabrication methods, suggesting that they can expand beyond conventional vacuum-based techniques to solution processes utilizing liquid sol–gel precursors such as spin coating, spray pyrolysis, and printing systems<sup>1,5</sup>. These processes offer advantages in cost-effective production over large areas compared to vacuum systems like sputtering and atomic layer deposition<sup>13</sup>. Since liquid precursors are used, it is possible to flexibly manipulate the composition of the sol–gel solution to obtain the desired characteristics of oxide films. Additionally, these techniques can be extended

<sup>1</sup>Department of Electrical Engineering and Computer Science, DGIST, Daegu, South Korea. <sup>2</sup>School of Electronic and Electrical Engineering, Kyungpook National University, Daegu, South Korea. <sup>3</sup>School of Electronics Engineering, Kyungpook National University, Daegu, South Korea. <sup>4</sup>Convergence Research Advanced Centre for Olfaction, DGIST, Daegu, South Korea. —e-mail: hj.kwon@dgist.ac.kr

to oxide electrodes. In cases where ternary to quaternary compounds or doping are required, such as for oxide electrodes, different precursors can be combined to synthesize the solution, enabling the fabrication of fully solution-processed oxide TFTs. Despite the potential of the solution processes, the decomposition of organic ligands within sol-gel-processed oxide films and the dense structuring of metal oxide networks typically involves a high-temperature annealing process of 400 °C or higher, which is generally incompatible with flexible substrates<sup>14</sup>. Hence, various methods, including UV or laser annealing, O2 annealing, and aqueous solvents, have been explored to form solution-processed oxide films at low temperatures, ensuring film quality and meeting the thermal requirements with flexible substrates<sup>15-19</sup>. These methods utilize processes such as changes in the energy source, selective energy delivery to localized areas, and reduction of the conversion temperature to oxides. Among these methods, combustion synthesis is a chemical process that utilizes the internal energy generated through the exothermic reaction of added organic fuel and oxidizer in the precursor, allowing for the elimination of organic residues and promoting the transition to oxide films even at reduced external temperatures<sup>20</sup>. This approach enables the production of high-quality oxide films at low temperatures without requiring extra systems. Additionally, it offers the flexibility to modify the composition of the solution or integrate it with other low-temperature fabrication methods for additional effects. In our previous studies, we manufactured SnO<sub>2</sub> TFTs using a combustion-assisted sol-gel process, achieving both oxide film formation and chlorine doping effect at low temperatures (~250 °C) by adjusting the composition of the solution used in the synthesis<sup>11,12</sup>. These results are compatible with flexible substrates, unlike Sn-based TFTs previously reported to be fabricated using the combustion process, which requires process temperatures of >350 °C<sup>21-23</sup>. Therefore, combustion synthesis can be a promising low-temperature sol-gel process for flexible SnO2 TFTs.

SiO<sub>2</sub> has been widely used as the gate dielectric in most oxide TFTs due to its wide bandgap and amorphous state, resulting in extremely low gate leakage current. However, these TFTs have faced operational difficulties at low driving voltages due to the low dielectric constant of SiO<sub>2</sub><sup>24</sup>. Furthermore, the thinning of the gate dielectric with the scaling down of electronic devices has led to high gate leakage currents. This has made it challenging to apply them to next-generation flexible devices that require both highperformance and low power consumption<sup>25</sup>. To address these challenges, high-k dielectrics, which allow a reduction in operating voltage and highdensity carrier accumulation through high capacitance values, have been proposed as new dielectric layers<sup>26</sup>. Among them, sol-gel-processed high-k oxides can be attractive alternatives, as they enable low-voltage operation and share the manufacturing process with sol-gel-processed oxide semiconductors. While various high-k oxides such as Al<sub>2</sub>O<sub>3</sub>, ZrO<sub>2</sub>, HfO<sub>2</sub>, and Y<sub>2</sub>O<sub>3</sub> have been reported to be manufactured through solution processes<sup>24,27–29</sup>, ZrO<sub>2</sub> has the potential to serve as an insulating layer in oxide TFTs for low-power operation due to its high dielectric constant (>20), sufficient bandgap (~5.8 eV), and electrical/chemical stability<sup>30</sup>. Furthermore, Zr<sup>4+</sup> (760 kJ/mol) demonstrates stronger bonding with oxygen compared to Al3+ (511 kJ/mol), which allows for the formation of more complete metal-oxygen bonds and enables a reduction in interface trap sites between the insulator and the semiconductor<sup>31,32</sup>. The oxygen vacancy within high-k dielectrics can serve as a source of carrier trap sites, leading to decreased mobility of TFTs or causing shifts in threshold voltage and increased gate leakage currents<sup>33</sup>. In particular, ZrO<sub>2</sub> has shown good compatibility with SnO<sub>2</sub> semiconductors, and previous ZrO<sub>2</sub>/SnO<sub>2</sub> TFTs manufactured through solution processes exhibited excellent dielectricsemiconductor interface properties and high electron mobility<sup>34</sup>. However, to obtain high-quality ZrO<sub>2</sub> films, high-temperature annealing (>400 °C) was still required. To fabricate ZrO<sub>2</sub>/SnO<sub>2</sub> TFTs on flexible substrates, both SnO<sub>2</sub> and ZrO<sub>2</sub> need to be manufactured using low-temperature solution processes. As mentioned earlier, we fabricated SnO<sub>2</sub> TFTs using combustion-assisted solution processes in our previous work. Combustion synthesis can be applied not only to SnO<sub>2</sub> but also to ZrO<sub>2</sub> for manufacturing at low temperatures. Moreover, the combination of ZrO<sub>2</sub> dielectric and  $SnO_2$  semiconductor fabricated from the same combustion materials enables the realization of sol-gel processed flexible oxide TFTs, while reducing processing times and costs.

In this paper, we report on high-performance flexible oxide TFTs realized with a SnO<sub>2</sub> semiconductor and high-k ZrO<sub>2</sub> dielectric formed at low temperatures using a combustion-assisted sol-gel process. Using the same approach as for the combustion of SnO<sub>2</sub> films, ZrO<sub>2</sub> films were formed at low temperatures. The external process temperature required to form the oxide network was estimated from thermogravimetric analysis (TGA). The structural and chemical composition differences of the prepared ZrO<sub>2</sub> films were confirmed by grazing incidence X-ray diffraction (GIXRD) and X-ray photoelectron spectroscopy (XPS). Compared to conventional ZrO<sub>2</sub> films, combustion films show an amorphous structure with a higher proportion of oxygen corresponding to the oxide network. These characteristics contribute to the low leakage current density and frequency-independent dielectric properties of combustion ZrO<sub>2</sub> films. We fabricated flexible ZrO<sub>2</sub>/ SnO<sub>2</sub> TFTs using combustion synthesis, and the fabricated flexible TFTs exhibited a field-effect mobility of 26.16 cm<sup>2</sup>/Vs, a subthreshold swing of 0.125 V/dec, and an on/off current ratio of  $1.13 \times 10^6$  at a low operating voltage of 3 V. Furthermore, we compared the changes in electrical characteristics during repetitive bending tests to confirm the impact of scaling effects on the mechanical flexibility of the TFTs. As the device dimensions decreased, the deterioration of electrical characteristics after bending tests was reduced, and stable TFT operation was observed even after 5000 cycles of bending tests with a bending radius of 2.5 mm. This is because relatively small devices are less likely to contain structural defects or microcracks induced by mechanical stress.

# Results and Discussion Design for combustion synthesis

In our previous work, we successfully deposited  $SnO_2$  films at low temperatures using combustion synthesis and fabricated  $SnO_2$  TFTs on  $Si/SiO_2$ , demonstrating enhanced TFT performance  $^{11,12}$ . Thermal analysis confirmed that the external temperature required for precursor conversion was 250 °C, significantly lower than that of conventional precursors. XPS spectra showed that the combustion  $SnO_2$  films had a more complete metal oxide network compared to conventional  $SnO_2$  films. Consequently, the combustion  $SnO_2$  TFTs exhibited significantly improved electrical performance compared to conventional  $SnO_2$  devices, with mobility increasing by approximately 170 times from 0.014 to 2.43 cm²/Vs and the subthreshold swing decreasing from 3.85 to 1 V/dec. This suggests the potential for the full realization of sol–gel processed  $SnO_2$ -based flexible TFTs, where low-temperature processes are required.

Figure 1 illustrates the process of forming  $ZrO_2/SnO_2$  films from combustion solutions. We prepared  $ZrO_2$  solutions using a combustion system similar to that of  $SnO_2$ . To synthesize these combustion  $ZrO_2$  solutions,  $Zr(C_5H_7O_2)_4$  was employed as the Zr source, while  $NH_4NO_3$  and  $CO(NH_2)_2$  were used as the oxidizer and fuel, respectively. For conventional  $ZrO_2$  films, high-temperature annealing is required because endothermic reactions dominate conventional sol–gel processed metal oxides. In contrast, combustion synthesis requires less external energy supply for the decomposition of organic ligands and the construction of oxide lattices due to the internally generated energy from exothermic reactions, compared to the conventional  $ZrO_2$  system. Therefore, combustion  $ZrO_2$  films can be manufactured at lower temperatures.

## Characteristics of ZrO<sub>2</sub> films

Figure 2a depicts the TGA curves of both ZrO<sub>2</sub> precursors, enabling an assessment of the energy necessary for their conversion to oxides. In TGA curves, the conversion temperature of the precursors is determined from the temperature range where the weight stabilizes with minimal changes. The combustion precursors experience a sharp drop of about 20% in weight at approximately 230 °C, followed by relatively minor weight changes. Conversely, conventional precursors display comparable curves below 200 °C but exhibit a gradual weight reduction without distinct variations. Hence,

**Fig. 1** | Schematic diagram illustrating the process for forming ZrO<sub>2</sub>/SnO<sub>2</sub> films using combustion solutions.

#### Combustion-assisted ZrO2/SnO2 films Metal source Oxidizer **Fuel** ZrO<sub>2</sub> solution Zr(C<sub>5</sub>H<sub>7</sub>O<sub>2</sub>)<sub>4</sub>NH<sub>4</sub>NO<sub>3</sub> CO(NH<sub>2</sub>)<sub>2</sub> SnCl<sub>2</sub>·2H<sub>2</sub>O SnO<sub>2</sub> solution Spin coating Combustion Spin coating **Annealing** Drying and annealing ZrO<sub>2</sub>/SnO<sub>2</sub> ₻ Repeat ZrO<sub>2</sub> film 150 °C 250 °C SnO<sub>2</sub> film (250 °C)

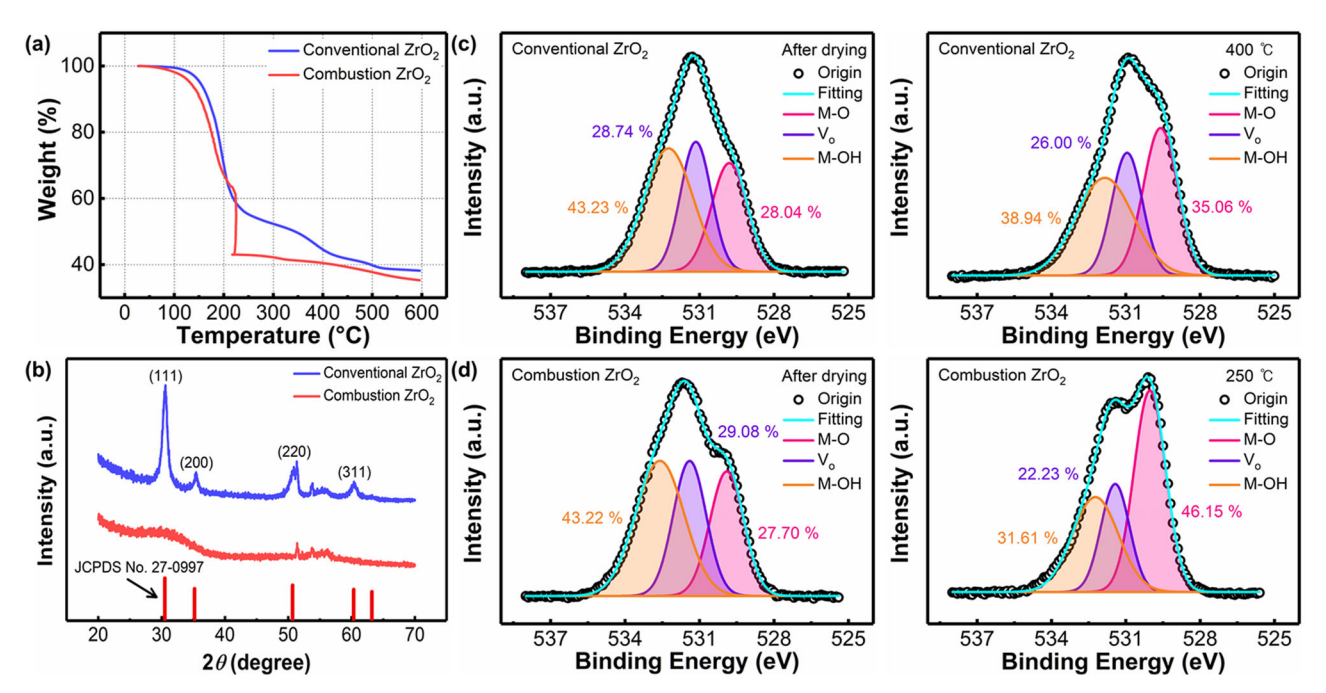


Fig. 2 | Characteristics of ZrO<sub>2</sub> films. a TGA spectra of ZrO<sub>2</sub> precursors with and without combustion materials. b GIXRD spectra of ZrO<sub>2</sub> films prepared from different precursors. XPS O 1 s spectra of c conventional and (d) combustion ZrO<sub>2</sub> films after the drying and annealing process.

from the TGA curves, it is discernible that combustion precursors primarily undergo conversion around 230 °C, whereas conventional precursors necessitate temperatures exceeding 400 °C. The TGA analysis indicates that the conversion of precursors in the combustion system occurs at significantly lower temperatures compared to conventional counterparts. This temperature difference suggests a reduced demand for external energy during oxide conversion, owing to the internal energy generated by the exothermic reaction of the combustion precursors. Using the conversion temperature obtained from thermal analysis as a reference, we determined that effective conversion into ZrO2 films could occur at 250 °C, similar to combustion SnO<sub>2</sub>. Furthermore, we anticipate that the resulting 2-terminal ZrO<sub>2</sub> devices may demonstrate enhanced performance compared to those produced using conventional precursors, which necessitate hightemperature annealing. Additional details regarding these expected results will be elaborated upon in the following section dedicated to electrical characteristics.

The structural characteristics of the  $ZrO_2$  films used as the dielectric in transistors have a significant impact on the gate leakage current of the fabricated devices. In particular, in polycrystalline dielectric layers, grain boundaries can lead to ion diffusion and act as leakage paths, potentially contributing to a significant increase in leakage current <sup>35,36</sup>. The GIXRD spectra obtained for the structurally analyzed  $ZrO_2$  films are presented in Fig. 2b. Both  $ZrO_2$  films exhibit minor peaks associated with the monoclinic

structure in the range of 50 to 60 degrees. The combustion  $\rm ZrO_2$  films do not show noticeable peaks in the provided GIXRD spectra, indicating an amorphous state. In contrast, the conventional  $\rm ZrO_2$  films annealed at 400 °C exhibit distinct peaks indicative of the cubic structure of  $\rm ZrO_2$  (JCPDS No. 27-0997). The peaks at 30.5°, 35.2°, 50.7°, and 60.3° imply the (110), (200), (220), and (311) crystal planes, respectively. As a result, they exhibit a polycrystalline structure with clear peaks, distinguishing them from combustion  $\rm ZrO_2$  films. The combustion  $\rm ZrO_2$  films subjected to 250 °C annealing reveal an amorphous state with no significant peaks, suggesting that low-temperature annealing presents obstacles to the crystalline growth of  $\rm ZrO_2$ . Considering these findings, combustion  $\rm ZrO_2$  films with an amorphous state, compared to high-temperature annealed crystalline  $\rm ZrO_2$  films, can contribute to suppressing the increase in leakage current associated with the grain boundaries.

We conducted an XPS analysis to investigate the changes in the oxygen composition of ZrO<sub>2</sub> films prepared using conventional and combustion precursors. The O 1 s spectra of the obtained ZrO<sub>2</sub> films are shown in Fig. 2c, d. These spectra have been separated into three binding energies at 529.9, 531.3, and 532.2 eV, corresponding to metal-oxygen lattice (M-O), oxygen vacancy (V<sub>o</sub>), and metal hydroxide (M-OH) groups<sup>37</sup>. Within solution-processed dielectrics, M-OH serves as an intermediate species that occurs before the formation of oxides. Therefore, a high M-O ratio indicates the formation of a more complete oxide lattice, while a high M-OH ratio

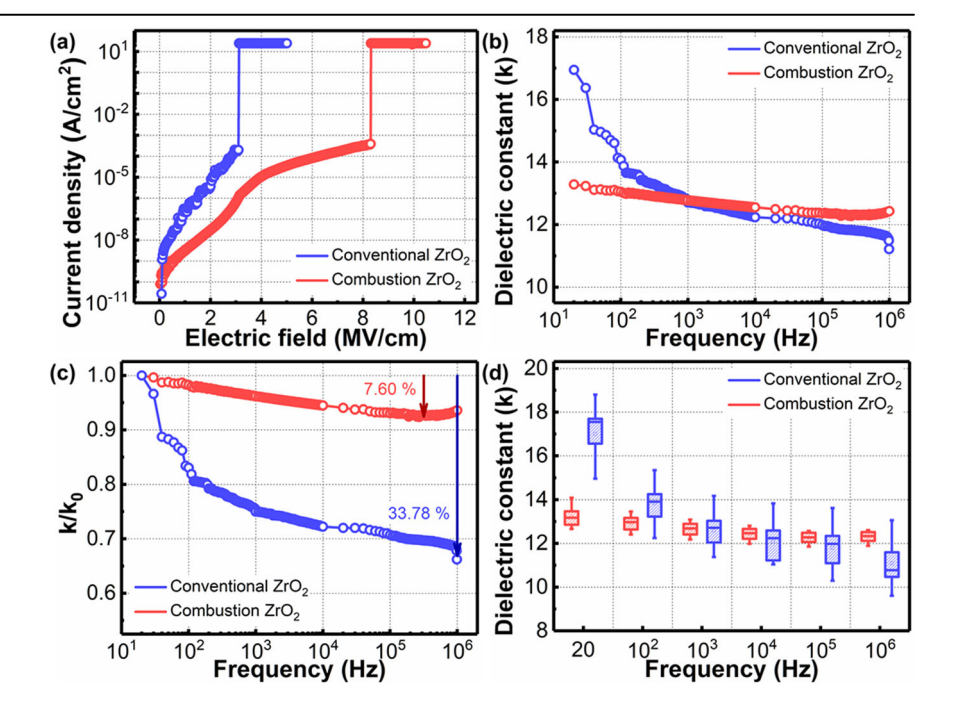
suggests incomplete precursor conversion due to inadequate energy supply. Additionally, they can act as trap sites, and dipolar groups like -OH often lead to frequency-dependent capacitance characteristics of dielectrics at low frequencies, along with impurities and mobile ions (H<sup>+</sup>)<sup>38</sup>. Also, V<sub>0</sub> is closely related to the increased leakage current characteristics of the insulator<sup>39,40</sup> Regardless of combustion synthesis, the dried ZrO2 films before thermal annealing exhibit low M-O, high Vo, and high M-OH ratios, indicating that insufficient thermal energy led to the incomplete formation of an oxide network. This is because the drying temperature (150 °C) is not high enough to induce the combustion reaction. As observed in the TGA analyses, the conversion temperature of the combustion precursors is 230 °C, which is higher than the drying temperature. Therefore, the combustion reaction is not triggered during the drying process, resulting in incomplete conversion to the oxide film and no significant difference in oxygen composition. Additionally, below 200 °C, both precursors exhibit similar weight loss curves, which is consistent with these results. After annealing, both ZrO2 films show an increase in the M-O ratio and a decrease in the V<sub>o</sub> and M-OH ratios compared to after drying. In particular, despite low-temperature annealing, the combustion ZrO2 films exhibit a higher M-O ratio, increasing from 35.06 to 46.15%, and lower  $V_{\rm o}$  and M-OH ratios compared to the conventional ZrO2 films annealed at 400 °C. These changes imply that ZrO2 films manufactured through combustion synthesis establish a more complete oxide network even with low-temperature annealing. This phenomenon can be attributed to the chemical energy released in the exothermic reaction of combustion precursors, facilitating precursor conversion and the condensation reactions between M-OH for oxide lattice formation even at low temperatures. Through previous TGA analysis, we confirmed that the conversion of combustion precursors mainly occurs at a much lower temperature, around 230 °C, compared to conventional systems. The TGA analysis aligns well with the XPS results of combustion ZrO<sub>2</sub> films, showing a more complete oxide network along with a high M-O ratio.

## Dielectric properties of ZrO<sub>2</sub> films

We manufactured metal-insulator-silicon (MIS) devices based on conventional and combustion  $ZrO_2$  to investigate the impact of combustion synthesis on the dielectric properties of  $ZrO_2$  films. Figure 3a presents leakage current density versus electric field plots for both conventional and combustion  $ZrO_2$  devices. The detailed leakage current density as a function of the electric field is summarized in Supplementary Table 1. The

conventional ZrO<sub>2</sub> films exhibit a breakdown field of ~3.1 MV/cm and leakage current density of  $\sim 2.82 \times 10^{-7} \,\mathrm{A/cm^2}$  at 1 MV/cm. However, the ZrO<sub>2</sub> films obtained through combustion synthesis show a significant increase in breakdown field to ~8.3 MV/cm, approximately 2.7 times higher, and a substantial reduction in leakage current density to  $\sim 3.06 \times 10^{-9}$  A/cm<sup>2</sup>, roughly 1/100 of the previous value, at 1 MV/cm. These values can be compared with previously reported vacuumprocessed oxide dielectrics, which demonstrated excellent insulating capabilities<sup>41-43</sup>. Figure 3b, c depict dielectric constant versus frequency curves and the variation of dielectric constants as a function of the frequency of ZrO2 films. The conventional ZrO2 films exhibit a high frequency dependence of dielectric constants, particularly in the lowfrequency range of 20 to 10<sup>3</sup> Hz. In contrast, the combustion ZrO<sub>2</sub> films show a dielectric constant of 13.22  $\pm$  0.43 at 20 Hz and a stable distribution of dielectric constants across the entire frequency range of 20 to 10<sup>6</sup> Hz. The decrease in dielectric constants across the whole frequency range is 7.6% for the combustion ZrO<sub>2</sub> films, whereas it is 33.78% for the conventional ZrO2 films, which is a notable difference. The statistical results and detailed values of dielectric constants as a function of frequency are shown in Fig. 3d and Supplementary Table 2. Supplementary Table 3 summarizes our results and the characteristics of ZrO2 dielectrics prepared using conventional vacuum deposition. The combustion ZrO<sub>2</sub> films exhibited properties such as low leakage current density and frequencyindependent dielectric constants, making them comparable to previously reported vacuum-processed ZrO2 films. The conventional ZrO2 films, exhibiting high frequency dependence, also show high dielectric constants at low frequencies, attributed to their higher M-OH ratio, which allows for easy absorption of highly polar water molecules<sup>44</sup>. These insulation and dielectric constant-frequency characteristics suggest that the combustion ZrO<sub>2</sub> films exhibit excellent dielectric properties in contrast to the conventional films annealed at high temperatures. Based on the GIXRD spectra, it was verified that the conventional ZrO<sub>2</sub> films exhibit a polycrystalline phase, while the combustion ZrO<sub>2</sub> films consist of an amorphous phase. As previously noted, the increase in leakage current associated with grain boundaries can be alleviated by the presence of the amorphous phase. Moreover, XPS results indicated that V<sub>0</sub>, associated with increased leakage current, is suppressed. Consequently, high-quality ZrO<sub>2</sub> films with a high M-O ratio were formed through the energy released from the combustion reaction. As a complete metal-oxygen network is

Fig. 3 | MIS devices fabricated with different ZrO<sub>2</sub> films. a Leakage current vs. electric field. b Dielectric constant, (c) variation in dielectric constant, and (d) statistical results of dielectric constant versus frequency (20 – 10<sup>6</sup> range).



established, the frequency dependence in capacitance induced by M-OH groups also decreases. Therefore, combining these film properties, combustion  ${\rm ZrO_2}$  films demonstrate enhanced dielectric properties compared to conventional films annealed at 400 °C.

### Electrical characteristics of ZrO<sub>2</sub>/SnO<sub>2</sub> TFTs

After verifying the dielectric properties of the fabricated combustion  $ZrO_2$  films, we proceeded to manufacture oxide TFTs capable of low-temperature and low-voltage operation using combustion  $SnO_2$  films. Figure 4 shows the schematics and electrical curves of the prepared TFTs. The transfer and output characteristics of combustion  $ZrO_2/SnO_2$  TFTs are shown in Fig. 4b, c. The TFTs operate at a low driving voltage of 3 V with a low gate leakage current of  $\sim\!10^{-9}$  A, demonstrating suitability for low-voltage operation oxide TFTs, owing to the prepared  $ZrO_2$  providing an amorphous phase and complete oxide network. The saturation mobility of  $ZrO_2/SnO_2$  TFTs was extracted from the following equation,

$$I_{DS} = \mu C_i \frac{W}{2L} (V_{GS} - V_{th})^2$$
 (1)

where C<sub>i</sub>, W, L, and V<sub>th</sub> represent the capacitance per unit area of the insulator, channel width, channel length, and threshold voltage, respectively. When extracting mobility, we used the dielectric constant obtained at the lowest frequency we could measure, which is 20 Hz, to suppress any overestimating mobility. The high frequency dependence commonly observed in dielectric constants due to hydroxyl groups and mobile ions in solution-processed dielectrics can lead to an overestimation of mobility in TFTs with high-k dielectrics<sup>45</sup>. The fabricated ZrO<sub>2</sub>/SnO<sub>2</sub> TFTs exhibited excellent electrical characteristics with a field effect mobility ( $\mu_{FF}$ ) of  $22.3 \pm 2.86$  cm<sup>2</sup>/Vs, a subthreshold swing (SS) of  $0.137 \pm 0.013$  V/dec, and an on/off current ratio ( $I_{on}/I_{off}$ ) of  $5.8 \times 10^5$ . Detailed statistical distribution of TFT parameters is shown in Supplementary Fig. 3. The extracted  $\mu_{FF}$ shows an improvement of about 10 times compared to the combustion SnO<sub>2</sub> TFTs fabricated on 100 nm thick SiO<sub>2</sub> layers in our previous work<sup>11,12</sup>. These results can be explained by the high carrier concentration achievable in the channel at low voltages due to high-k dielectrics, along with the shallow donor-like states in the ZrO2 layers that provide additional electrons<sup>46</sup>. As localized trap sites that hinder carrier transport become filled with accumulated carriers, it leads to improved mobility and better band-like transport of the  $\rm ZrO_2/SnO_2$  devices<sup>20,34</sup>. Generally, solution-processed oxide semiconductors exhibit amorphous or polycrystalline states, leading to localized trap states within the energy band and consequently following a trap-dependent multiple trapping and release (MTR) model<sup>47,48</sup>. However, when trap sites are filled, the transport mechanism transitions from MTR to a percolation conduction (PC) model, demonstrating band-like transport<sup>45</sup>. To verify the transport model governing the  $\rm ZrO_2/SnO_2$  TFT, the  $\mu_{FE}$  was fitted to an integrated power-law equation including the gate voltage below:

$$\mu_{FE} = K(V_G - V_{T,P})^{\gamma}, \gamma = 2\left(\frac{T_c}{T} - 1\right)$$
 (2)

where K and y correspond to the nature of carrier transport. Supplementary Fig. 4 shows the results of fitting the mobility of combustion ZrO<sub>2</sub>/SnO<sub>2</sub> TFTs to the equation above. The value of  $\gamma$  in the above equation provides insight into the dominant transport model for the respective oxide TFTs, with  $\gamma$  values close to 0.7 and 0.1 in MTR and PC models, respectively<sup>47</sup>. Combustion ZrO<sub>2</sub>/SnO<sub>2</sub> TFTs exhibit different y values at low and high  $V_{GS}$ . At low  $V_{GS}$ , the  $\gamma$  for combustion TFTs was 0.70, while at high  $V_{GS}$ , the  $\gamma$  values were 0.12. The variation in  $\gamma$  indicates the shift of dominant carrier transport from MTR to PC models as the gate voltage increases. The weak dependence of mobility on VGS also serves as evidence of the transition to the PC model. Additionally, the overestimated mobility obtained from conventional MOSFET analysis can be addressed by applying a scaling factor of  $1/\gamma + 1$ , which reflects the transport models of metal oxides<sup>49</sup>. The accurate mobility of oxide TFTs can be derived by multiplying the mobility obtained through conventional methods by this scaling factor. The scaling factors for combustion ZrO<sub>2</sub>/SnO<sub>2</sub> TFTs are 0.59 at low V<sub>GS</sub> and 0.89 at high V<sub>GS</sub>, respectively. Improved results are also observed in the SS, which is correlated with the trap density at the dielectric-semiconductor interface. As the dielectric layers shift from SiO<sub>2</sub> to ZrO<sub>2</sub>, the average SS values show a steeper slope, from 1 to 0.137 V/dec. This suggests a lower trap density at the ZrO<sub>2</sub>/SnO<sub>2</sub> interface, which is consistent with the significantly improved mobility observed in the ZrO<sub>2</sub>/SnO<sub>2</sub> devices. The surface morphology of the combustion ZrO<sub>2</sub> films obtained through atomic force microscopy (AFM) measurements can be seen in Supplementary Fig. 1e, and the

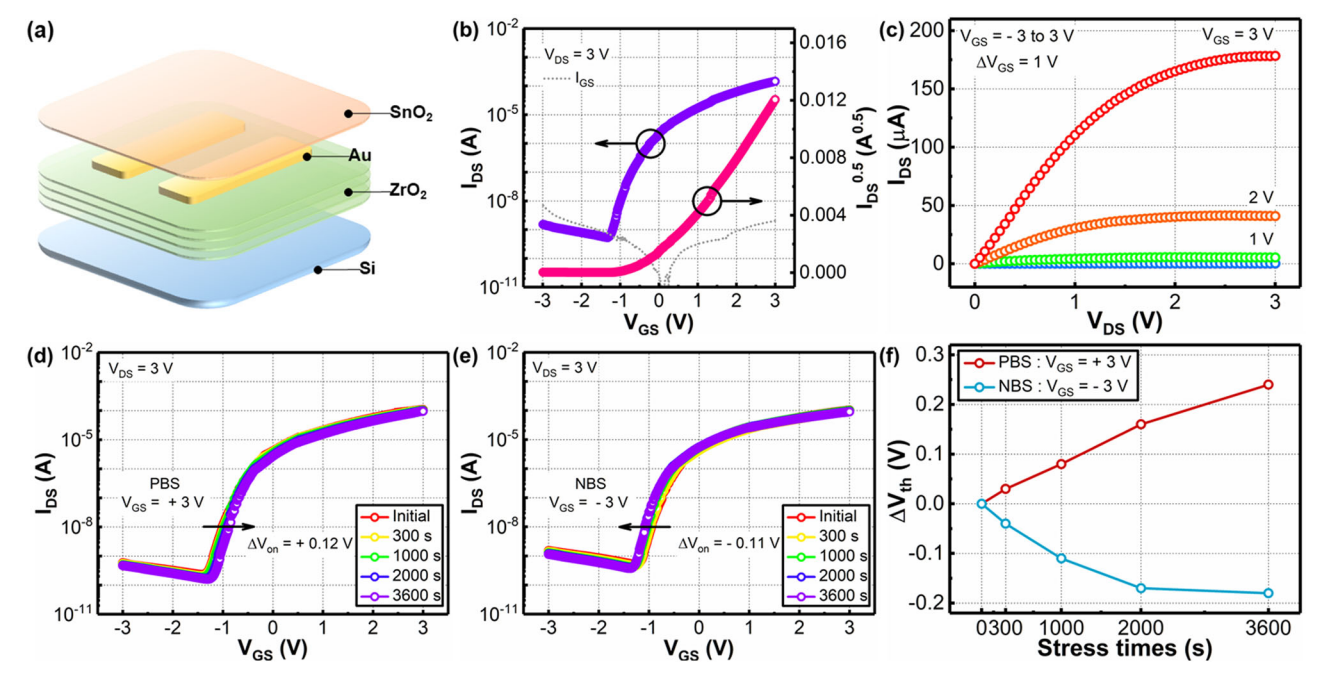


Fig. 4 | Electrical characteristics of ZrO<sub>2</sub>/SnO<sub>2</sub> TFTs. a Schematic diagram of the fabricated ZrO<sub>2</sub>/SnO<sub>2</sub> TFT structures. b Transfer and (c) output characteristics of the devices. Transfer characteristics of the devices under(d) PBS, and (e) NBS. f V<sub>th</sub> shift as a function of stress time under PBS and NBS.

root-mean-square (RMS) roughness of the prepared ZrO2 films was measured to be 0.563 nm, indicating a very smooth surface. This smoothness helps improve carrier transport and prevents degradation in device performance caused by rough dielectric-semiconductor interfaces. Electrical stability is also a crucial factor in TFT performance and should be considered for the practical use of solution-processed oxide TFTs. Figure 4d, e exhibit the transfer characteristics of the TFT under positive bias stress (PBS) and negative bias stress (NBS), while Fig. 4f shows the shift in V<sub>th</sub> as a function of stress time. During the stress time of 3600 s considered for monitoring the stability of most oxide TFTs reported previously<sup>50-52</sup>, our device exhibited a shift of + 0.22 V under PBS and -0.18 V under NBS. The V<sub>th</sub> shift induced by NBS can be seen to be relatively smaller compared to PBS. As seen in Fig. 4a, this is associated with the exposed SnO<sub>2</sub> layers of the fabricated devices. Unlike NBS, which is primarily influenced by trap sites at the dielectric-semiconductor interface<sup>53,54</sup>, PBS is caused by oxygen species being absorbed through the back channel in ambient conditions<sup>55,56</sup>.

# Mechanical stability of flexible TFTs

After confirming the excellent electrical characteristics of  $\rm ZrO_2/SnO_2$  TFTs fabricated on rigid substrates, we proceeded to manufacture high-performance, low-voltage operation  $\rm ZrO_2/SnO_2$  TFTs on flexible substrates. We fabricated flexible  $\rm ZrO_2/SnO_2$  TFTs with various channel sizes and aligned the gate and source/drain (S/D) electrodes to minimize overlap during the fabrication process. The schematics and optical images of the prepared  $\rm ZrO_2/SnO_2$  TFTs can be seen in Fig. 5a, b, and detailed images for each channel size are shown in Fig. 5d–f. It is crucial for flexible TFTs to demonstrate stable electrical characteristics under mechanical stress. To compare the mechanical flexibility varying with the device's dimensions, we applied repetitive tensile stress with a bending radius of 2.5 mm for 5000 cycles to the flexible TFTs, as shown in Fig. 5c, and observed changes in their electrical characteristics. The strain applied to our TFT structure can be estimated using the following equation:

$$\varepsilon = \frac{Y_{TFT} - Y_c}{\rho} \tag{3}$$

where  $Y_{TFT}$  is distance from the bottom of the polyimide (PI) film to the center of the TFT layer,  $Y_c$  is the position of neutral plane for stacked films,

and  $\rho$  is the bending radius. The position of the neutral plane is calculated using the following equation<sup>57</sup>:

$$Y_c = \frac{\sum_i Y_i E_i t_i}{\sum_i E_i t_i} \tag{4}$$

$$Y_i = \left(\sum_{j=1}^i t_j\right) - \frac{t_i}{2} \tag{5}$$

where  $E_i$  and  $t_i$  are the Young's modulus and thickness of the i-th layer, respectively, and  $Y_i$  is the distance from the bottom of the stacked films to the center of the i-th layer. The Young's modulus of each layer in the flexible TFT, based on previously reported values, is shown in Supplementary Table 4. The position of the neutral plane, calculated from these values, is  $\sim 26.93 \ \mu m$  from the bottom of the stacked films. The strain at the TFT location, estimated using equation (3), is approximately 0.53% with a bending radius of 2.5 mm.

We successfully fabricated enhancement-mode flexible ZrO<sub>2</sub>/SnO<sub>2</sub> TFTs on PI substrates. Figure 6a-c depicts the transfer characteristics of ZrO<sub>2</sub>/SnO<sub>2</sub> TFTs with different channel sizes during the bending test, while Supplementary Table 5 shows the parameters of the flexible TFTs before and after the bending test. The fabricated flexible  $ZrO_2/SnO_2$  TFTs (W/L = 200/ 20  $\mu$ m) exhibited excellent electrical characteristics with a  $\mu_{EE}$  of  $26.16 \pm 1.73 \text{ cm}^2/\text{Vs}$ , a SS of  $0.125 \pm 0.005 \text{ V/dec}$ , and an  $I_{on}/I_{off}$  of  $1.13 \times 10^6$ , showing enhanced  $\mu_{FE}$  compared to devices fabricated on rigid substrates. This improvement can be attributed to the increased charge carrier injection due to the change in the configuration of the flexible TFTs to bottom gate top contact, as opposed to the bottom gate bottom contact structure used in TFTs fabricated on rigid substrates. Additionally, the flexible ZrO2/SnO2 TFTs show a significant shift in V<sub>th</sub> compared to the TFTs on rigid substrates and operate in enhancement mode. To elucidate the changes in operation modes, we obtained an energy band diagram, and Supplementary Fig. 5 illustrates the energy band diagram of the gate, ZrO<sub>2</sub> dielectric, and SnO<sub>2</sub> semiconductor. The position of the Fermi level (E<sub>F</sub>) within the energy band of the SnO<sub>2</sub> film was estimated using the bandgap derived from the UV-vis spectra (Supplementary Fig. 5a) and the energy level difference between the E<sub>F</sub> and the valence band maximum (E<sub>VBM</sub>) obtained from the XPS spectra at the valence

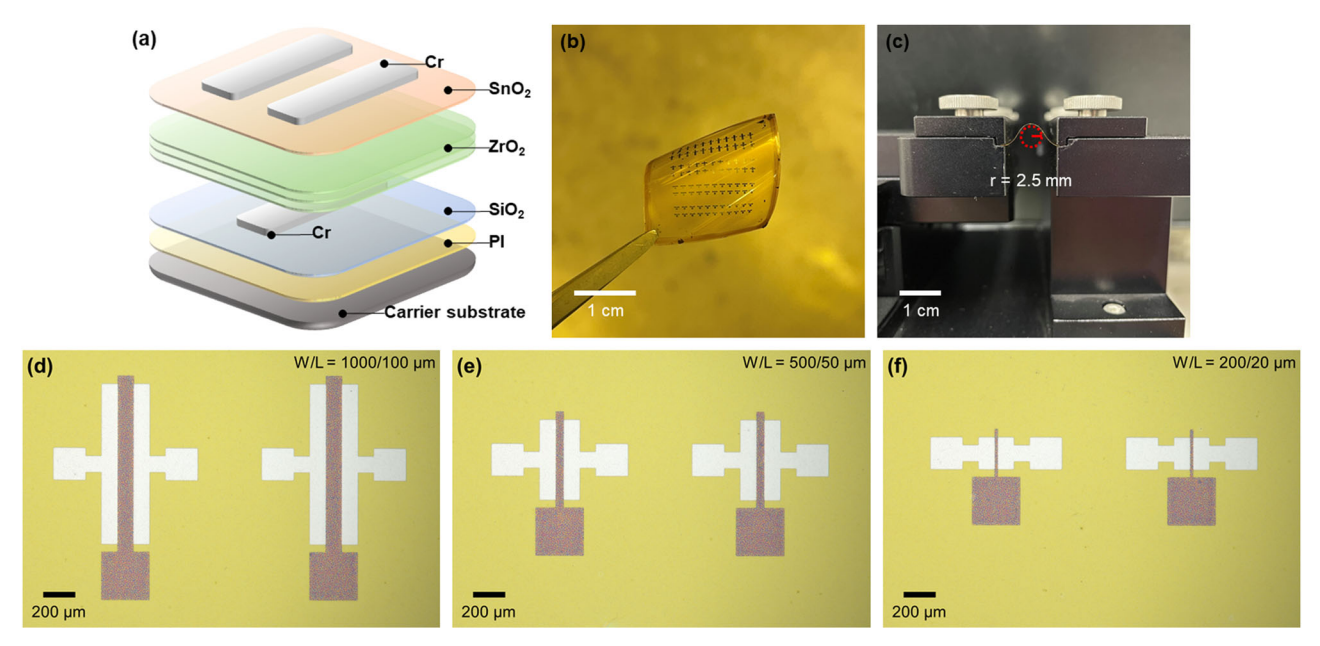
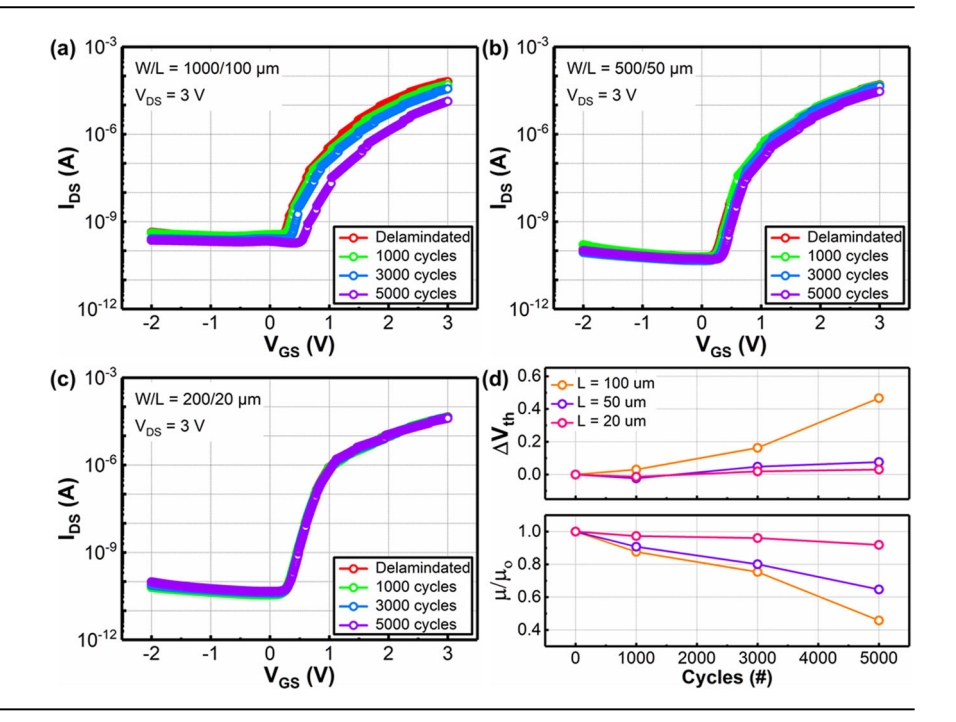


**Fig. 5 | Flexible ZrO<sub>2</sub>/SnO<sub>2</sub> TFTs. a** Schematics of the fabricated ZrO<sub>2</sub>/SnO<sub>2</sub> TFTs on PI substrates. **b** Optical images of flexible ZrO<sub>2</sub>/SnO<sub>2</sub> TFTs. **c** Optical images of flexible TFTs in the bending state for mechanical stress testing. Optical microscopy

images of flexible TFTs with different L: (d) 100, (e) 50, and (f) 20  $\mu$ m, while maintaining a constant W/L ratio.

Fig. 6 | Electrical characteristics of flexible ZrO<sub>2</sub>/SnO<sub>2</sub> TFTs. Transfer characteristics of ZrO<sub>2</sub>/SnO<sub>2</sub> TFTs under bending stress for 5000 cycles at a 2.5 mm radius, varying with different L: (a) 100, (b) 50, and (c) 20  $\mu$ m, while maintaining a consistent W/L ratio. d  $\mu$ <sub>FE</sub> and V<sub>th</sub> variation under bending cycles.



band region (Supplementary Fig. 5b). Subsequently, this was compared to the work functions of  $n^{++}$  Si and Cr when used as gate electrodes. From the energy band diagram in Supplementary Fig. 5c, d, these changes in  $V_{th}$  can be explained by the increased work function difference between the gate and the semiconductor, resulting from the change in the gate electrode of the flexible TFTs from n++ Si to Cr, compared to TFTs fabricated on rigid substrates.

The flexible TFTs exhibit variations in characteristics depending on the channel size. Shorter channel devices exhibit relatively decreased  $\mu_{FE}$ compared to devices with longer channels, due to the influence of contact resistance<sup>58,59</sup>. Although these devices are fabricated from the same materials, as the channel length decreases, the channel resistance decreases, and consequently, the proportion of contact resistance in the total resistance increases. As a result, the effective voltage drop across the channel region decreases, leading to a decrease in  $\mu_{FE}$ . As the channel size decreases, a reduction in SS is observed, indicating an improvement in the quality of the interface between the semiconductor and insulator. Smaller TFTs can have fewer defects at the interface area, resulting in a reduction in trapped electrons at the interface trap sites<sup>60</sup>. The increased electrons lead to a negative shift in V<sub>th</sub>, consistent with the decrease in V<sub>th</sub> in the smallest devices. Furthermore, the reduced interface trap sites lead to a low off current<sup>61</sup>, thereby increasing the I<sub>on</sub>/I<sub>off</sub>. The electrical characteristics of the fabricated flexible TFTs can be compared to previously reported vacuum or solutionprocessed high-k dielectric flexible oxide TFTs, and their mobility is fully compatible with state-of-the-art high-resolution active matrix displays (see Supplementary Table 6)<sup>62</sup>.

We investigated the mechanical properties of TFTs by comparing the electrical characteristics before and after the bending test, with particular attention to the scaling effect. As seen in Fig. 6 (a), TFTs with the largest channel sizes (1000/100  $\mu m$ ) clearly exhibit a decrease in on current along with the shift of the transfer curve during the bending cycles. Figure 6d and Supplementary Fig. 6 show the variations in TFT parameters depending on the bending cycles of devices with different channel sizes. Large-sized devices exhibit a noticeable decrease in  $\mu_{FE}$  and a clear positive shift in V<sub>th</sub> during bending tests. After 5000 cycles, V<sub>th</sub> shifts positively from 1.27 to 1.65 V, and the  $\mu_{FE}$  decreases to 46% of its original value, while SS increases from 0.148 to 0.154 V/dec. Repetitive bending cycles induce structural defects or microcracks in areas such as the gate dielectric-semiconductor interface or the gate electrode-gate dielectric interface where stress concentrates  $^{61}$ . These changes can be explained by stress-induced structural defects trapping carriers at the ZrO<sub>2</sub> and SnO<sub>2</sub> interfaces. The increased interface trap density

due to structural defects degrades the interface quality, reduces the carrier concentration in the channel region, and leads to the an increase in SS and a positive shift in V<sub>th</sub> <sup>64,65</sup>. Additionally, from the perspective of the oxide carrier transport model (i.e. MTR), the increased localized trap sites hinder carrier transport, resulting in reduced  $\mu_{FE}$  and degraded band-like transport. The accumulated defects during bending tests accelerate these changes. Also, microcracks formed during the bending test may propagate parallel to the bending direction, potentially leading to a decrease in mobility due to the presence of microcracks in the semiconductor layer<sup>64</sup>. However, as the channel size decreases, the shift in the transfer curve and performance degradation after the bending test are reduced, and in the TFT with the smallest size (see Fig. 6c), V<sub>th</sub> barely changed from 1.04 to 1.09 V, while the mobility remained at 92% compared to before bending. Also, SS and I<sub>on</sub>/I<sub>off</sub> show nearly constant values. This indicates that stable flexible TFTs have been implemented to withstand mechanical stress, suggesting that the dimensions of the devices influence the mechanical flexibility of TFTs. Relatively small-sized devices can withstand mechanical stress better compared to larger ones because it is more challenging for structural defects or microcracks induced by bending tests to be incorporated into the reduced insulating and channel regions. Furthermore, as seen in Fig. 5, the dimensions of the patterned electrodes, particularly the gate electrode, also decrease as the device dimensions decrease. Smaller patterned electrodes are less likely to develop microcracks under mechanical bending stress, thereby further enhancing the mechanical properties of the TFTs<sup>57</sup>. Supplementary Fig. 7 shows optical images of flexible TFTs after the bending test. Supplementary Fig. 7a shows microcracks induced by mechanical stress, which are more likely to be contained within the region of a relatively larger TFT. Additionally, as seen in Supplementary Fig. 7b, c, noticeable cracks due to bending stress are observed in larger gate electrodes compared to smaller ones, which correspond to changes in the mechanical properties depending on the electrode pattern size. Therefore, as seen in our results, as the dimension of devices decreases, the changes in transfer characteristics and main TFT parameters noticeably decrease. In particular, the smallest devices (200/20 µm) demonstrated robust mechanical stability, even under repeated bending stress, along with excellent TFT performance.

In this paper, we implement high-performance  $ZrO_2/SnO_2$  TFTs on flexible substrates by combining  $SnO_2$  semiconductors and  $ZrO_2$  dielectrics obtained through a combustion-assisted sol-gel process. The internal energy generated from the oxidizer and organic fuel added for combustion synthesis aids in forming metal oxide networks even at low process

temperatures. We fabricated ZrO<sub>2</sub> films at low temperatures using the same approaches as for our previous combustion SnO<sub>2</sub> films, and we confirmed the reduced conversion temperature compared to the conventional precursor through TGA. The GIXRD and XPS O 1 s spectra revealed that the combustion ZrO<sub>2</sub> films exhibit an amorphous phase, with a low proportion of V<sub>o</sub> and OH groups and a high proportion of oxygen corresponding to the metal oxide network. Two-terminal MIS devices fabricated with combustion ZrO<sub>2</sub> exhibited higher breakdown voltages and lower leakage current density compared to conventional ZrO2 devices. Additionally, a lower frequency dependence of the dielectric constant was observed. This is attributed to the amorphous phase and decreased V<sub>o</sub> and polar OH groups. The fabricated ZrO<sub>2</sub>/SnO<sub>2</sub> TFTs on rigid substrates showed excellent electrical characteristics, including a  $\mu_{FF}$  of 22.3 cm<sup>2</sup>/Vs, a SS of 0.137 V/dec, and an  $I_{on}/I_{off}$  of  $5.8 \times 10^5$  at a low operating voltage of 3 V. These results can be explained by the better band-like transport resulting from the filling of localized trap sites with high-density carriers achieved at low voltages using high-k dielectrics. After confirming the promising TFT performance of ZrO<sub>2</sub>/SnO<sub>2</sub> devices, we successfully realized enhancement-mode flexible  $ZrO_2/SnO_2$  TFTs on PI substrates. The fabricated TFTs exhibited a  $\mu_{FE}$  of 26.16 cm<sup>2</sup>/Vs, a SS of 0.125 V/dec, and an  $I_{on}/I_{off}$  of  $1.13 \times 10^6$ , showing enhanced  $\mu_{FE}$  compared to devices fabricated on rigid substrates. This result can be explained by the increased work function of the gate electrode in flexible TFTs compared to those fabricated on rigid substrates, along with the structural change to bottom gate top contact, leading to increased carrier injection. We confirmed the scaling effect on the mechanical properties of TFTs by comparing the electrical performance through repetitive bending cycles. As the device dimensions decreased, the changes in transfer characteristics and performance degradation after bending tests reduced. This is because relatively small devices are less likely to contain structural defects or microcracks induced by mechanical stress. Furthermore, the smallest TFT demonstrated robust mechanical stability by withstanding 5000 cycles of bending tests at a bending radius of 2.5 mm. Therefore, combustion synthesis can be employed as a suitable process for the mass production of sol-gel process-based metal oxide electronic and flexible devices.

#### Methods

# Synthesis of combustion ZrO<sub>2</sub> and SnO<sub>2</sub> precursors

We used ZrO<sub>2</sub> and SnO<sub>2</sub> precursors to form the dielectric and semiconductor layers of oxide TFTs. First, for the ZrO2 layers, we synthesized clear 0.1 M zirconium solutions by dissolving 0.001 mol of zirconium acetylacetonate  $(Zr(C_5H_7O_2)_4)$  in 10 ml of ethanol and subjecting it to ultrasonication for 1 h. The conventional ZrO<sub>2</sub> films were obtained by annealing the zirconium solution without adding extra additives. Next, to prepare the combustion ZrO<sub>2</sub> precursors, ammonium nitrate (NH<sub>4</sub>NO<sub>3</sub>) and urea (CO(NH<sub>2</sub>)<sub>2</sub>), serving as an oxidizer and fuel, were added to the prepared zirconium solutions, with 0.001 mol of each component. Since Zr(C<sub>5</sub>H<sub>7</sub>O<sub>2</sub>)<sub>4</sub> does not contain NO<sub>3</sub> ions to serve as an oxidizer, NH<sub>4</sub>NO<sub>3</sub> containing NO<sub>3</sub> was added. In a combustion system, the fuel is ignited by a relatively low level of external energy, providing internal chemical energy, and the NO<sub>3</sub> contained in NH<sub>4</sub>NO<sub>3</sub> acts as an oxidizer, leading to the activation of the combustion reaction, which is a form of redox reaction. Then, we stirred and aged the prepared combustion ZrO2 solutions at 80 °C for 48 hr to obtain a homogeneous yellowish solution. Next, the combustion SnO2 solutions were prepared using a process similar to that of ZrO2 solutions. Tin (II) chloride dihydrate (SnCl<sub>2</sub>·2H<sub>2</sub>O) was dissolved in ethanol to synthesize 0.04 M of SnO<sub>2</sub> precursors. Then, NH<sub>4</sub>NO<sub>3</sub> and CO(NH<sub>2</sub>)<sub>2</sub> were added in a 1:1 ratio to SnCl<sub>2</sub>·2H<sub>2</sub>O as an oxidizer and fuel for the combustion precursors. Subsequently, the resulting solution was stirred and aged at room temperature for 72 h to obtain homogeneous combustion SnO<sub>2</sub> solutions.

#### Fabrication process of ZrO<sub>2</sub> devices and ZrO<sub>2</sub>/SnO<sub>2</sub> TFTs

We manufactured 2-terminal  $ZrO_2$  MIS structures to measure the electrical properties of  $ZrO_2$  films. For the MIS devices,  $ZrO_2$  solutions were spin-coated onto heavily n-doped Si at 3000 rpm for 50 s, followed by 1 min drying at 150 °C to form the  $ZrO_2$  layers. This process was repeated to

control the thickness of the ZrO2 layers. Before coating, the Si wafers underwent a 10 min UV/Ozone treatment for surface energy control. In addition to electrical characterization, we performed photopatterning to determine the thickness of the prepared ZrO<sub>2</sub> films. Shadow masks were applied onto the dried ZrO2 layers and exposed to UV light for 10 min, followed by rinsing with DI water to pattern the ZrO2 films. The photopatterning of ZrO<sub>2</sub> films is attributed to the photoreaction induced by UV irradiation of the metal precursors. In the UV-exposed areas, the precursors use light energy to form partial metal-oxygen bonds, whereas the unexposed areas, due to the shadow mask, do not undergo precursor conversion and are removed during rinsing with DI water. This results in the formation of ZrO<sub>2</sub> patterns corresponding to the UV exposure. The prepared combustion ZrO<sub>2</sub> films were annealed at 250 °C for 1 h, resulting in a film thickness of ~80 nm. Finally, top electrodes were deposited onto the patterned ZrO<sub>2</sub> layers using a thermal evaporator to fabricate the MIS structures. The area dimensions of the top electrodes are 120 × 120 µm<sup>2</sup> with a thickness of 50 nm. The details of the photopatterned ZrO<sub>2</sub> films and MIS structure are shown in Supplementary Fig. 1.

The combustion ZrO<sub>2</sub>/SnO<sub>2</sub> TFTs were fabricated through a process similar to the MIS structure. ZrO<sub>2</sub> solutions were spin-coated onto heavily n-doped Si under the same conditions and annealed at 250 °C. Before forming the SnO<sub>2</sub> layer, the S/D electrodes were patterned through a lift-off process. Au or Au/Cr layers were deposited using a thermal evaporator, and the resulting electrodes have a W and L of 1000  $\mu m$  and 100  $\mu m$ , respectively. The SnO<sub>2</sub> films were formed by coating SnO<sub>2</sub> solutions onto the ZrO<sub>2</sub> at 3000 rpm for 50 s, followed by annealing at 250 °C for 1 h to manufacture the ZrO<sub>2</sub>/SnO<sub>2</sub> TFTs. Before the annealing process, mechanical removal of the coated films along the deposited electrodes was performed to reduce fringe and leakage currents.

#### Fabrication process of flexible ZrO<sub>2</sub>/SnO<sub>2</sub> TFTs

We fabricated flexible ZrO<sub>2</sub>/SnO<sub>2</sub> TFTs on PI substrates. The fabrication process is as follows; Before coating PI, poly(vinyl alcohol) (PVA) was utilized as a sacrificial layer on the carrier substrate to facilitate easy detachment of PI. A solution prepared by dissolving 0.1 g of PVA in 40 ml of DI water was spin-coated onto the carrier substrate at 2000 rpm for 30 s and then dried at 110 °C for 90 s. Subsequently, the PI solution was spin-coated onto the PVA layer at 3000 rpm for 30 sec and dried at 90 °C for 5 min. This process was repeated to control the thickness of the PI layer, followed by annealing at 300 °C for 30 min for thermal solidification. The obtained thickness of PI was ~40 μm. Next, to compensate for the thermal mismatch between the PI layer and the ZrO2 layers, PECVD-SiO2 (100 nm) buffer layers were deposited, and Cr (50 nm) was deposited as the bottom gate electrode on the SiO<sub>2</sub>. Supplementary Fig. 2 illustrates the ZrO<sub>2</sub> surface variation with the presence of a buffer layer. As shown in Supplementary Fig. 2a, cracks occurred during the annealing of ZrO<sub>2</sub> coated on the PI substrate. This issue arises from thermal stress due to the mismatch in thermal expansion coefficients between the oxide films and polymer substrates<sup>66</sup>. To alleviate this thermal mismatch, we introduced SiO<sub>2</sub>, which had been used as a buffer layer in various oxide films, into our structure<sup>67-69</sup>. The ZrO<sub>2</sub> surface annealed on top of the buffer layer showed a crack-free appearance, as depicted in Supplementary Fig. 2b. In bottom-gate structure TFTs, the requirement for the gate electrode is adhesion with the flexible substrate. Taking this into consideration, we chose Cr as the bottom gate electrode. Subsequently, the ZrO2 and SnO2 layers were deposited as the dielectric and semiconductor layers, respectively, and Cr (50 nm) was deposited as the S/D electrodes to fabricate bottom-gate, top-contact TFTs. To confirm the scaling effect, the sizes of the flexible TFT channels were prepared in three different sizes, maintaining a W/L ratio of 10 with L = 100, 50, and 20 µm. After the process, the PI film was immersed in DI water to dissolve the PVA and delaminate it from the carrier substrate.

#### Characterization of ZrO<sub>2</sub> films and TFTs

The thermal behavior of the prepared ZrO<sub>2</sub> precursors was analyzed using TGA (TA Instruments/Discovery SDT 650). TGA analyses were

conducted on approximately 20 mg samples obtained from evaporated precursor solutions. The samples were heated at a rate of 10 °C/min with a 30 ml/min airflow using a platinum sample pan. The differences in crystallinity and structural characteristics of  $ZrO_2$  films fabricated from different precursors were determined using GIXRD (Panalytical/Empyrean) with Cu Kα radiation ( $\lambda=1.54~\textrm{Å}$ ). Surface morphology of the  $ZrO_2$  films and thickness measurements of the patterned  $ZrO_2$  films were performed using AFM (Park Systems/NX-10). XPS (Thermo Scientific/ESCALAB 250Xi) analysis with a monochromatic Al Kα (1488 eV) source was conducted to investigate the oxygen composition within the formed  $ZrO_2$  films. The electrical properties of the fabricated MIS devices and  $ZrO_2/SnO_2$  TFTs were measured using the Keithley 4200-SCS analysis system inside a probe station.

# **Data availability**

The data that support the findings of this study are available from the corresponding author upon reasonable request.

Received: 16 July 2024; Accepted: 20 October 2024; Published online: 02 November 2024

#### References

- Shi, J. et al. Wide bandgap oxide semiconductors: from materials physics to optoelectronic devices. Adv. Mater. 33, 2006230 (2021).
- Liu, K., Ouyang, B., Guo, X., Guo, Y. & Liu, Y. Advances in flexible organic field-effect transistors and their applications for flexible electronics. npj Flex. Electron. 6, 1 (2022).
- Mirshojaeian Hosseini, M. J. & Nawrocki, R. A. A review of the progress of thin-film transistors and their technologies for flexible electronics. *Micromachines* 12, 655 (2021).
- 4. Song, J. et al. Recent developments of flexible InGaZnO thin-film transistors. *Phys. Status Solidi A* **218**, 2000527 (2021).
- Park, J. W., Kang, B. H. & Kim, H. J. A review of low-temperature solution-processed metal oxide thin-film transistors for flexible electronics. *Adv. Funct. Mater.* 30, 1904632 (2020).
- Xia, G. & Wang, S. Rapid and facile low-temperature solution production of ZrO<sub>2</sub> films as high-k dielectrics for flexible low-voltage thin-film transistors. *Ceram. Int.* 45, 16482–16488 (2019).
- Jin, J. et al. Low-voltage, high-performance, indium-tin-zinc-oxide thin-film transistors based on dual-channel and anodic-oxide. Adv. Electron. Mater. 9, 2201117 (2023).
- Kim, H., Maeng, S., Lee, S. & Kim, J. Improved performance and operational stability of solution-processed InGaSnO (IGTO) thin film transistors by the formation of Sn–O complexes. ACS Appl. Electron. Mater. 3, 1199–1210 (2021).
- Zhang, M. et al. The investigation of indium-free amorphous Zn-Al-Sn-O thin film transistor prepared by magnetron sputtering. *Coatings* 11, 585 (2021).
- Jenifer, K., Arulkumar, S., Parthiban, S. & Kwon, J. A review on the recent advancements in tin oxide-based thin-film transistors for largearea electronics. J. Electron. Mater. 49, 7098–7111 (2020).
- Jang, B., Jang, J., Jang, J. E. & Kwon, H.-J. Combustion-assisted low-temperature solution process for high-performance SnO<sub>2</sub> thin-film transistors. *Ceram. Int.* 48, 20591–20598 (2022).
- Jang, B., Lee, J., Kang, H., Jang, J. & Kwon, H.-J. Schottky barrier modulation of bottom contact SnO<sub>2</sub> thin-film transistors via chloridebased combustion synthesis. *J. Mater. Sci. Technol.* 148, 199–208 (2023).
- Jang, B., Kim, J., Lee, J., Jang, J. & Kwon, H.-J. Stable switching behavior of low-temperature ZrO<sub>2</sub> RRAM devices realized by combustion synthesis-assisted photopatterning. *J. Mater. Sci. Technol.* 189, 68–76 (2024).
- Palneedi, H. et al. Laser irradiation of metal oxide films and nanostructures: applications and advances. *Adv. Mater.* 30, 1705148 (2018).

- Kim, Y.-H. et al. Flexible metal-oxide devices made by roomtemperature photochemical activation of sol-gel films. *Nature* 489, 128–132 (2012).
- Pan, H. et al. Melt-mediated coalescence of solution-deposited ZnO nanoparticles by excimer laser annealing for thin-film transistor fabrication. Appl. Phys. A 94, 111–115 (2009).
- Yeo, J. et al. Laser-induced hydrothermal growth of heterogeneous metal-oxide nanowire on flexible substrate by laser absorption layer design. ACS nano 9, 6059–6068 (2015).
- Faber, H. et al. Heterojunction oxide thin-film transistors with unprecedented electron mobility grown from solution. Sci. Adv. 3, e1602640 (2017).
- Hwan Hwang, Y. et al. An 'aqueous route' for the fabrication of lowtemperature-processable oxide flexible transparent thin-film transistors on plastic substrates. NPG Asia Mater. 5, e45 (2013).
- Kim, M.-G., Kanatzidis, M. G., Facchetti, A. & Marks, T. J. Low-temperature fabrication of high-performance metal oxide thin-film electronics via combustion processing. *Nat. Mater.* 10, 382–388 (2011).
- Han, Y.-J. et al. Performance improvement of ZnSnO thin-film transistors with low-temperature self-combustion reaction. *Electronics* 10, 1099 (2021).
- 22. Salgueiro, D. et al. Solution based zinc tin oxide TFTs: The dual role of the organic solvent. *J. Phys. D: Appl. Phys.* **50**, 065106 (2017).
- Li, J. et al. Amorphous LaZnSnO thin films by a combustion solution process and application in thin film transistors. *Electron. Mater. Lett.* 12, 76–81 (2016).
- Wang, B. et al. High-k gate dielectrics for emerging flexible and stretchable electronics. Chem. Rev. 118, 5690–5754 (2018).
- Zhang, Q. et al. High-performance Zinc-Tin-Oxide thin film transistors based on environment friendly solution process. *Curr. Appl. Phys.* 19, 174–181 (2019).
- Liu, A., Zhu, H., Sun, H., Xu, Y. & Noh, Y. Y. Solution processed metal oxide high-κ dielectrics for emerging transistors and circuits. Adv. Mater. 30, 1706364 (2018).
- 27. Wang, B. et al. Solution-processed all-oxide transparent high-performance transistors fabricated by spray-combustion synthesis. *Adv. Electron. Mater.* **2**, 1500427 (2016).
- Esro, M., Vourlias, G., Somerton, C., Milne, W. I. & Adamopoulos, G. High-mobility ZnO thin film transistors based on solution-processed hafnium oxide gate dielectrics. Adv. Funct. Mater. 25, 134–141 (2015).
- Cho, Y.-J., Shin, J.-H., Bobade, S., Kim, Y.-B. & Choi, D.-K. Evaluation of Y<sub>2</sub>O<sub>3</sub> gate insulators for a-IGZO thin film transistors. *Thin Solid Films* 517, 4115–4118 (2009).
- Panda, D. & Tseng, T.-Y. Growth, dielectric properties, and memory device applications of ZrO<sub>2</sub> thin films. *Thin Solid Films* 531, 1–20 (2013).
- 31. Dean, J. A. Lange's handbook of chemistry. (1999).
- Islam, M. M. et al. Solution-processed la alloyed ZrO<sub>x</sub> high-k dielectric for high-performance ZnO thin-film transistors. *IEEE Electron Device Lett.* 41, 1021–1024 (2020).
- Mohsenifar, S. & Shahrokhabadi, M. Gate stack high-κ materials for Si-based MOSFETs past, present, and futures. *Terminology* 2, 5 (2015).
- 34. Jang, J. et al. Transparent high-performance thin film transistors from solution-processed SnO<sub>2</sub>/ZrO<sub>2</sub> gel-like precursors. *Adv. Mater.* **25**, 1042–1047 (2013).
- 35. Gieraltowska, S. et al. Characterization of dielectric layers grown at low temperature by atomic layer deposition. *Thin Solid Films* **577**, 97–102 (2015).
- McKenna, K. et al. Grain boundary mediated leakage current in polycrystalline HfO<sub>2</sub> films. *Microelectron. Eng.* 88, 1272–1275 (2011).
- Huang, W. et al. Ultraviolet light-densified oxide-organic selfassembled dielectrics: processing thin-film transistors at room temperature. ACS Appl. Mater. Interfaces 13, 3445–3453 (2021).

- Sil, A. et al. Role of fluoride doping in low-temperature combustionsynthesized ZrO<sub>x</sub> dielectric films. ACS Appl. Mater. Interfaces 14, 12340–12349 (2022).
- Chang, T.-J. et al. High-K gate dielectrics treated with in situ atomic layer bombardment. ACS Appl. Electron. Mater. 1, 1091–1098 (2019).
- Huang, K.-W. et al. Leakage current lowering and film densification of ZrO<sub>2</sub> high-k gate dielectrics by layer-by-layer, in-situ atomic layer hydrogen bombardment. *Mater. Sci. Semicond. Process.* 109, 104933 (2020).
- 41. Kim, J. et al. Low leakage in high-k perovskite gate oxide SrHfO<sub>3</sub>. *Adv. Electron. Mater.* **9**, 2201341 (2023).
- Liu, J., Li, J., Wu, J. & Sun, J. Structure and dielectric property of high-k ZrO<sub>2</sub> films grown by atomic layer deposition using tetrakis (dimethylamido) zirconium and ozone. *Nanoscale Res. Lett.* 14, 1–12 (2019).
- Shahin, D. I. et al. Electrical characterization of ALD HfO<sub>2</sub> high-k dielectrics on (2<sup>-</sup>01) β-Ga<sub>2</sub>O<sub>3</sub>. Appl. Phys. Lett. 112, (2018).
- Xu, W. et al. Facile and environmentally friendly solution-processed aluminum oxide dielectric for low-temperature, high-performance oxide thin-film transistors. ACS Appl. Mater. Interfaces 7, 5803–5810 (2015).
- Kim, D.-K. et al. Viable strategy to minimize trap states of patterned oxide thin films for both exceptional electrical performance and uniformity in sol–gel processed transistors. Chem. Eng. J. 441, 135833 (2022).
- Sun, Y., Kim, J., Chatterjee, N. & Swisher, S. L. Investigation of the determining factors for the "Mobility Boost" in high-k-gated transparent oxide semiconductor thin-film transistors. *Adv. Electron. Mater.* 7, 2001037 (2021).
- Lee, S. et al. Trap-limited and percolation conduction mechanisms in amorphous oxide semiconductor thin film transistors. *Appl. Phys. Lett.* 98, (2011).
- Lee, C.-G., Cobb, B. & Dodabalapur, A. Band transport and mobility edge in amorphous solution-processed zinc tin oxide thin-film transistors. *Appl. Phys. Lett.* 97, (2010).
- Lee, S., Nathan, A., Ye, Y., Guo, Y. & Robertson, J. Localized tail states and electron mobility in amorphous ZnON thin film transistors. Sci. Rep. 5, 13467 (2015).
- Park, H., Nam, Y., Jin, J. & Bae, B.-S. Improvement of bias stability of oxyanion-incorporated aqueous sol–gel processed indium zinc oxide TFTs. J. Mater. Chem. C. 2, 5998–6003 (2014).
- Shiah, Y.-S., Sim, K., Ueda, S., Kim, J. & Hosono, H. Unintended carbon-related impurity and negative bias instability in high-mobility oxide TFTs. *IEEE Electron Device Lett.* 42, 1319–1322 (2021).
- Ok, K.-C. et al. The effects of buffer layers on the performance and stability of flexible InGaZnO thin film transistors on polyimide substrates. Appl. Phys. Lett. 104, (2014).
- Gwang Um, J., Mativenga, M., Migliorato, P. & Jang, J. Increase of interface and bulk density of states in amorphous-indium-galliumzinc-oxide thin-film transistors with negative-bias-under-illuminationstress time. *Appl. Phys. Lett.* 101, (2012).
- Kwon, J. M., Jung, J., Rim, Y. S., Kim, D. L. & Kim, H. J. Improvement in negative bias stress stability of solution-processed amorphous In–Ga–Zn–O thin-film transistors using hydrogen peroxide. ACS Appl. Mater. Interfaces 6, 3371–3377 (2014).
- Yun, M. G., Kim, S. H., Ahn, C. H., Cho, S. W. & Cho, H. K. Effects of channel thickness on electrical properties and stability of zinc tin oxide thin-film transistors. *J. Phys. D: Appl. Phys.* 46, 475106 (2013).
- Jeong, J. K., Won Yang, H., Jeong, J. H., Mo, Y.-G. & Kim, H. D. Origin of threshold voltage instability in indium-gallium-zinc oxide thin film transistors. *Appl. Phys. Lett.* 93, (2008).
- Lee, S., Jeong, D., Mativenga, M. & Jang, J. Highly robust bendable oxide thin-film transistors on polyimide substrates via mesh and strip patterning of device layers. Adv. Funct. Mater. 27, 1700437 (2017).
- Cho, E. N., Kang, J. H. & Yun, I. Contact resistance dependent scalingdown behavior of amorphous InGaZnO thin-film transistors. *Curr. Appl. Phys.* 11, 1015–1019 (2011).

- Hu, S. et al. High mobility amorphous indium-gallium-zinc-oxide thinfilm transistor by aluminum oxide passivation layer. *IEEE Electron Device Lett.* 38, 879–882 (2017).
- Xiao, D.-Q. et al. High performance (V<sub>th</sub>~0 V, SS~69 mV/dec, I<sub>Or</sub>/I<sub>Off</sub>~10<sup>10</sup>) thin-film transistors using ultrathin indium oxide channel and SiO<sub>2</sub> passivation. *IEEE Trans. Electron Devices* 69, 3716–3721 (2022).
- Han, L. et al. Eliminating leakage current in thin-film transistor of solution-processed organic material stack for large-scale low-power integration. Adv. Electron. Mater. 8, 2200014 (2022).
- 62. Shin, H.-J. et al. in SID Symp. Dig. Tech. Pap. 611-614 (Wiley Online Library).
- 63. Ning, H. et al. Transparent flexible IGZO thin film transistors fabricated at room temperature. *Membranes* **12**, 29 (2021).
- 64. Heng, J., Park, J., Choi, D. W., Lim, J. & Park, J. S. A study on the electrical properties of atomic layer deposition grown InO<sub>x</sub> on flexible substrates with respect to N<sub>2</sub>O plasma treatment and the associated thin-film transistor behavior under repetitive mechanical stress. ACS Appl. Mater. Interfaces 8, 31136–31143 (2016).
- Jeong, H.-J., Han, K.-L., Jeong, K.-S., Oh, S. & Park, J.-S. Effects of repetitive mechanical stress on flexible oxide thin-film transistors and stress reduction via additional organic layer. *IEEE Electron Device Lett.* 39, 971–974 (2018).
- Daunis, T. B., Schroder, K. A. & Hsu, J. W. Photonic curing of solutiondeposited ZrO<sub>2</sub> dielectric on PEN: a path towards high-throughput processing of oxide electronics. npj Flex. Electron. 4, 7 (2020).
- Kim, H. K. & Mathur, M. Thermally stable ZnO films deposited on GaAs substrates with a SiO<sub>2</sub> thin buffer layer. *Appl. Phys. Lett.* 61, 2524–2526 (1992).
- Kim, H. M. et al. Low-resistivity SrRuO<sub>3</sub> thin films formed on SiO<sub>2</sub> substrates without buffer layer by RF magnetron sputtering. *J. Alloy. Compd.* 857, 157627 (2021).
- Stognij, A. et al. Growth of Y<sub>3</sub>Fe<sub>5</sub>O<sub>12</sub> films on Si with AlO<sub>x</sub> and SiO<sub>2</sub> buffer layers by ion beam sputtering. *Inorg. Mater.* 53, 1069–1074 (2017).

# **Acknowledgements**

This work was supported by the National Research Foundation of Korea (NRF) funded by the Ministry of Science and ICT (MSIT) (RS-2024-00428887 and 2022M3D1A2083618).

# **Author contributions**

B.J. designed the research and wrote the manuscript. J.K., J.L., G.P., and G.Y. supported the experiments and data analysis. J.J. and H.K. supervised the research. H.K. was responsible for managing all aspects of this project and fundings. All the authors discussed the results and commented on the manuscript.

# **Competing interests**

The authors declare no competing interests.

# **Additional information**

**Supplementary information** The online version contains supplementary material available at https://doi.org/10.1038/s41528-024-00362-8.

**Correspondence** and requests for materials should be addressed to Hyuk-Jun Kwon.

**Reprints and permissions information** is available at http://www.nature.com/reprints

**Publisher's note** Springer Nature remains neutral with regard to jurisdictional claims in published maps and institutional affiliations.

Open Access This article is licensed under a Creative Commons Attribution-NonCommercial-NoDerivatives 4.0 International License, which permits any non-commercial use, sharing, distribution and reproduction in any medium or format, as long as you give appropriate credit to the original author(s) and the source, provide a link to the Creative Commons licence, and indicate if you modified the licensed material. You do not have permission under this licence to share adapted material derived from this article or parts of it. The images or other third party material in this article are included in the article's Creative Commons licence, unless indicated otherwise in a credit line to the material. If material is not included in the article's Creative Commons licence and your intended use is not permitted by statutory regulation or exceeds the permitted use, you will need to obtain permission directly from the copyright holder. To view a copy of this licence, visit <a href="http://creativecommons.org/licenses/by-nc-nd/4.0/">http://creativecommons.org/licenses/by-nc-nd/4.0/</a>.

© The Author(s) 2024